

Automatic detection of microaneurysms in color fundus images

Thomas Walter ^{a,*}, Pascale Massin ^b, Ali Erginay ^b, Richard Ordonez ^a,
Clotilde Jeulin ^a, Jean-Claude Klein ^a

^a Center of Mathematical Morphology, 35 Rue St.Honoré, 77300 Fontainebleau, France

^b Service d'Ophthalmologie, Hôpital Lariboisière 2, rue Ambroise-Paré, 75010 Paris, France

Received 21 March 2006; received in revised form 16 April 2007; accepted 9 May 2007

Available online 26 May 2007

Abstract

This paper addresses the automatic detection of microaneurysms in color fundus images, which plays a key role in computer assisted diagnosis of diabetic retinopathy, a serious and frequent eye disease.

The algorithm can be divided into four steps. The first step consists in image enhancement, shade correction and image normalization of the green channel. The second step aims at detecting candidates, i.e. all patterns possibly corresponding to MA, which is achieved by diameter closing and an automatic threshold scheme. Then, features are extracted, which are used in the last step to automatically classify candidates into real MA and other objects; the classification relies on kernel density estimation with variable bandwidth.

A database of 21 annotated images has been used to train the algorithm. The algorithm was compared to manually obtained gradings of 94 images; sensitivity was 88.5% at an average number of 2.13 false positives per image.

© 2007 Elsevier B.V. All rights reserved.

Keywords: Microaneurysm detection; Diabetic retinopathy; Diameter opening; Attribute opening; Criteria based operators; Mathematical morphology; Lesion detection; Shade correction; Density estimation

1. Introduction

Diabetic retinopathy (DR) is one of the most serious and most frequent eye diseases in the world; it is the most common cause of blindness in adults between 20 and 60 years of age. DR is a complication of *diabetes mellitus* and although the disease does not necessarily coincide with vision impairment, about 2% of the diabetic patients are blind and 10% suffer from vision loss after 15 years of diabetes (Klein et al., 1995; Massin et al., 2000) due to DR complications.

Moreover, due to the increasing number of diabetic patients, the number of people affected by DR is expected to increase; DR has become a serious problem for our society and for the public health system. According to Lee et al. (2001), blindness due to diabetic eye disease produces costs of about 500 million dollars a year in the United States.

The main cause of the disease is the elevation of glucose in the blood, resulting in an alteration of the vascular walls whose first manifestations are microaneurysms (MA), tiny dilations of the capillaries. They can be seen as the first unequivocal sign of DR. This first abnormality does not affect the vision itself, but progression of DR to later stages leads to complications such as new vessels and macular edema, possibly leading to vision impairment and blindness. Both of these two main complications can be prevented by a proper treatment if the disease is detected early enough. Hence, early diagnosis of DR is essential for the prevention of vision impairment and blindness threatening a large number of persons in our society.

One of the easiest ways to diagnose DR is the analysis of color fundus images: their acquisition is cheap, non-invasive and easy to perform, and the most important lesions of DR are visible in this type of images. Although fluorescein angiographies (FA) allow detection of MA with a greater sensitivity, they are invasive and costly and therefore not adapted for screening purposes.

* Corresponding author.

E-mail address: Thomas.Walter@cmm.ensmp.fr (T. Walter).

As DR is a silent disease in its first stages, i.e. many patients are not aware of its presence, it often remains undiagnosed until serious vision impairment occurs (Klein et al., 1992). Annual examinations of all diabetic patients are therefore highly recommended (Klein et al., 1995; Lee et al., 2001). The problem is however that this would produce tremendous costs, because the number of examinations would be enormous. Over and above that, there are not enough specialists to perform so many examinations; especially in rural areas, a mass-screening of DR is not feasible at present. An automatic pre-diagnosis based on image processing may help to overcome this problem by identifying automatically all “abnormal” retinas, i.e. all color images showing typical lesions for DR (Massin, 2002).

A further field of actual problems in the diagnosis of DR is the quantitative evaluation of different examinations in order to assess the evolution of the disease. At present, this is mostly done qualitatively. MA counts are a good indicator for the progression of DR (Klein et al., 1995; Hellstedt and Immonen, 1996; Massin et al., 2000) and can therefore be used for quantitative diagnosis. The aspect of quantification is extremely important for the efficiency assessment of a treatment or of a new drug. However, a manual comparison between different images is a very time-consuming and error-prone task. Once again, computer assisted diagnosis may help to overcome this problem (Zana, 1999).

As MA are the first unequivocal sign of DR as well as an indicator for its progression (Massin et al., 2000), their automatic detection plays a key role for both, mass-screening and monitoring and is therefore in the core of any system for computer assisted diagnosis of DR. In this paper, we present in detail a method for the automatic detection of MA, which has been developed in a mass-screening framework, without being limited to it. We do not present, in this article, a complete screening or monitoring system. A screening system usually contains other lesion detection algorithms, as well as an additional classification layer. A monitoring system requires, in addition to the automatic lesion detection, a robust registration algorithm.

The paper is structured as follows: First, we present former approaches for MA detection in color fundus images and angiographies. Then, we describe our method for automatic detection of MA based on criteria closings and kernel density estimation for automatic classification. Finally, we discuss the results of the algorithm.

2. State of the art

As the detection of MA is crucial to computer assisted diagnosis of DR, there is a large number of publications addressing this problem. Most of these publications deal with the detection of MA in fluorescein angiographies. The problem is similar: in the green channel of color images, MA appear as dark patterns, small, isolated and of circular shape. In FA, they appear as bright patterns and better contrasted, but the shape characteristics remain the same.

The first algorithm for the detection of MA in FA has been presented in 1983 by Laÿ (1983). The author introduced the radial opening $\gamma^{\text{sup}} = \cup \gamma^{L_i}$, i.e. the supremum of morphological openings with linear structuring elements L_i in different directions in order to remove the MA but to preserve the piecewise linear vessels. The difference image (the so-called top-hat transformation) $f - \gamma^{\text{sup}}(f)$ extracts details which may correspond to MA. Variants of this technique have been used subsequently by most of the authors working on the automatic detection of MA.

Spencer et al. (1991) propose a shade correction and a normalization of the dynamic range. The candidates are detected by means of a matched filter approach. This candidate filter is not well adapted to distinguish between MA and elongated structures, which is done in a second step.

Øien and Osnes (1995) propose a quite similar prefiltering procedure; the candidates are found by morphological hit and miss transform. Even if this approach was not further investigated, it was the first publication dealing with the detection of MA in color images.

Spencer et al. (1996) propose more advanced image correction procedures for FA (using additional control images) as well as a more complete and more efficient MA detection algorithm; they were the first to propose an additional classification step (rule based) after the top-hat based segmentation. They also showed the limits of the method presented in Laÿ (1983), which will be discussed later on.

In Spencer et al. (1996), Frame et al. (1998), and Mendonça et al. (1999) variations of this method are proposed; namely the prefiltering and classification procedures are improved or changed. A much more sophisticated classification method has been proposed in Autio et al. (2005).

In Walter and Klein (2002), Walter (2003), criteria based closings have been applied for candidate segmentation; as classification method, the KNN method was used. These were former versions of the algorithm presented in this paper.

In Niemeijer et al. (2005), the authors aim at detecting MA and hemorrhages with a similar method, but with a segmentation step based on pixel classification. The strength of this method lies in the detection of larger lesions for which there is no information about size and shape (like hemorrhages). In order not to miss too many MA, they make use of a hybrid strategy combining their method with (Spencer et al., 1996; Frame et al., 1998).

3. An automatic method for the detection of MA in color fundus images

MA appear as small reddish isolated patterns of circular shape in color fundus images (Massin et al., 2000). They are characterized by their diameter which is always smaller than 125 μm . As they are situated on capillaries, and as capillaries are not visible in color fundus images, they appear as isolated patterns, i.e. disconnected from the vascular tree.

MA have typically low contrast and they may be hard to distinguish from noise or pigmentation variations.

The pipeline of the method presented in this paper is illustrated in Fig. 1. First, a shade correction algorithm is applied to the green channel in order to remove slow background variations due to non-uniform illumination. Then, candidates are detected by means of the diameter closing (Walter and Klein, 2002) and an automatic threshold scheme. In a third step, features are calculated for these candidates allowing the final decision whether they are to be accepted as real MA or rejected. As classification procedure, we use Bayesian risk minimization with kernel based density estimation (Fricout and Jeulin, 2004; Webb, 2002; Duda and Hart, 1973).

In this study, we used an image set of 115 uncompressed digital images taken with a SONY color video 3CCD camera on a Topcon TRC NW6 retinograph with dilatation of the pupil. The images have a size of 640×480 with circular ROI, a resolution of $13.6 \mu\text{m}$ per pixel and they have been taken with an angle of 45° . The algorithm parameters we give refer to these images. In the following, we will detail and discuss each step of the algorithm, but first, we will discuss the color content of fundus images.

3.1. Use of color information

In publications concerning fundus image analysis, it can often be read that the green channel is the most contrasted one, that the red channel is saturated and that the blue channel does not contain any information. In this subsection, we want to make a few remarks on this observation; a more detailed discussion can be found in Walter and Klein (2005) and Moreno Barriuso (2000).

In Preece and Claridge (2001), and Delori and Pflibsen (1989), an interpretation of the color content of fundus images is given, based on a radiation transport model. After having entered the inner eye through the pupil, the light transverses its different layers where it is partly reflected, absorbed and transmitted. The percentages of reflected, absorbed and transmitted light depend on the tissue properties and in particular on the concentration of the two pigments melanin and hemoglobin.

The violet and blue light entering the eye is mostly absorbed by the lens pigments. Also, the absorption coefficients of melanin and hemoglobin for blue light are higher than for other wavelengths; as a consequence, most of the blue light is absorbed within the eye and does not contribute much to the spectrum of a color fundus image. Over and above that, the dispersion of blue light is higher than for light of higher wavelengths. That is why opacities disturb blue light more than light of lower frequency.

For green light, there is a particular situation because the absorption coefficient of hemoglobin has a peak in this part of the spectrum. As a consequence, features containing hemoglobin absorb more green light than the surrounding tissue; they appear dark and well contrasted in images taken with green light. The green light is reflected on the retinal pigment epithelium and the choroid.

Green light is less absorbed by the fundus layers than the blue part of the spectrum, but more than red light, which penetrates deeper into the layers of the inner eye and which is mainly reflected in the choroid. The red light is less absorbed by the pigments of the inner eye, and it dominates the reflected spectrum. This is the reason why the color fundus images appear reddish. Because of the lower absorption coefficients for red light, structures containing pigments are less contrasted than it is the case for green light. Furthermore, the remitted spectrum for red light depends much on melanin concentration in the choroid, as shown in Preece and Claridge (2001).

These considerations explain the observations made by many authors, that the green channel of the RGB-representation shows the best contrast, that the red channel is often saturated (or at least the brightest color channel) and has low contrast, and that the blue channel is very noisy and suffers from poor dynamic range. This does not mean that there cannot be any useful information in the red and blue channel. It just means that blood containing elements (as MA or vessels) in the retinal layer are best represented and have highest contrast in the green channel.

3.2. Preprocessing

Color fundus images often suffer from non-uniform illumination, poor contrast and noise. The preprocessing step aims at attenuating these imperfections.

In this subsection, we present an operator which performs shade correction and contrast enhancement. We start by defining a global contrast operator and show that its local application results in a shade correction operator. Darkening due to bright lesions is taken into consideration; a filtering step has been proposed in order to avoid it. This operator has first been proposed in Walter (2003), a variation of this operator has then been published in Niemeijer et al. (2005).

3.2.1. Polynomial contrast enhancement

The polynomial contrast enhancement operator is a simple gray level transformation: it assigns to each pixel a new gray level independently of the neighbor gray level distribution.

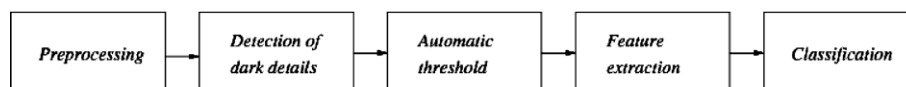


Fig. 1. Steps of MA detection.

Let $f: E \rightarrow T$ be a gray level image with $T = \{t_{\min}, \dots, t_{\max}\} \subset \mathbb{R}$ a set of rational numbers. Let $U = \{u_{\min}, \dots, u_{\max}\} \subset \mathbb{R}$ be a second set of rational numbers. A gray level transformation Γ is a mapping $T \rightarrow U$, $u = \Gamma(t)$.

We define a polynomial gray level transformation with parameter r as follows:

$$u = \Gamma(t) = \begin{cases} a_1 \cdot (t - t_{\min})^r + b_1 & \text{if } t \leq \mu_f, \\ a_2 \cdot (t - t_{\max})^r + b_2 & \text{if } t > \mu_f \end{cases} \quad (1)$$

with a_1, a_2, b_1, b_2 a set of parameters which can be determined in order to obtain a convenient transformation graph, and μ_f the global gray level mean of image f .

For convenience, the gray level transformation is constructed in such a way that it assigns the center between u_{\min} and u_{\max} to the mean value μ_f , i.e.:

$$\lim_{t \rightarrow \mu_f^-} \Gamma(t) = \lim_{t \rightarrow \mu_f^+} \Gamma(t) = \frac{1}{2}(u_{\min} + u_{\max}). \quad (2)$$

Furthermore, it makes sense to postulate $\Gamma(t_{\min}) = u_{\min}$ and $\Gamma(t_{\max}) = u_{\max}$ in order to make use of the whole range of U . With these four conditions, we can determine a_1, a_2, b_1 and b_2 of Eq. (1), and we obtain for the global polynomial contrast enhancement operator:

$$u = \Gamma(t) = \begin{cases} \frac{\frac{1}{2}(u_{\max} - u_{\min})}{(\mu_f - t_{\min})^r} \cdot (t - t_{\min})^r + u_{\min} & \text{if } t \leq \mu_f, \\ -\frac{\frac{1}{2}(u_{\max} - u_{\min})}{(\mu_f - t_{\max})^r} \cdot (t - t_{\max})^r + u_{\max} & \text{if } t > \mu_f. \end{cases} \quad (3)$$

The corresponding graph is shown in Fig. 2 for different μ_f . The resulting transformation is not necessarily symmetric to the point $(\mu_f, \frac{1}{2}(u_{\max} + u_{\min}))$.

With parameter r , which can be chosen freely, we can control how much the contrast is enhanced. Suppose that $\mu_f = \frac{1}{2}(t_{\min} + t_{\max})$. Then, we obtain a linear contrast stretching operator for $r = 1$. For $r \rightarrow \infty$, we apply the threshold μ_f .

If this operator is applied to the whole image as a global contrast operator, the result is not satisfying due to slow

background variation. In fact, the proposed gray level transformation does only enhance the contrast for subsets of T for which $\frac{\partial u}{\partial t} > 1$ (see Fig. 2). For instance, the contrast of a dark detail situated in a dark region may even be attenuated.

3.2.2. Contrast enhancement and shade correction

It is possible however to overcome this problem by applying the contrast operator of Eq. (3) locally, i.e. we substitute the global mean μ_f by a local background approximation. One possibility is to calculate the mean value of f within a window W centered in the pixel x :

$$\mu_f^W(x) = \frac{1}{N_W} \sum_{\xi \in W(x)} f(\xi). \quad (4)$$

As for large window sizes, this operator would be very slow, it is advantageous to make use of *integral images* (Papageorgiou et al., 1998; Viola and Jones, 2004). The window size in our study was chosen 25×25 pixels; r was chosen to be 2.

In this way, a contrast operator is obtained for which the transformation parameters depend on the mean value of the image in a sliding window of a certain size. Hence, besides enhancing the contrast, this operator also removes slow background variations, because the contrast enhancement graph from Fig. 2 is readjusted in every point to the local mean.

However, for pixels close to bright features, the background approximation may be biased by blurred bright objects. Indeed, we observe a “darkening” close to bright objects as the papilla or exudates (see Fig. 3b). This darkening is a real problem in MA segmentation. Therefore we propose to calculate the local mean value on a filtered image, where all these bright features have been removed. The area opening γ_λ^a (Vincent, 1992) removes all bright objects having an area (number of pixels) smaller than λ (we have chosen $\lambda = 2500$); it preserves the contours of the remaining objects. As the contour preservation is crucial in this case, this operator seems well adapted to this task. For readability, we write μ^* for the mean value of the area opened image $\gamma_\lambda^a f$ within a window W , i.e. $\mu^* = \mu_{\gamma_\lambda^a f}^W(x)$, and we obtain:

$$[SC(f)](x) = \begin{cases} \frac{\frac{1}{2}(u_{\max} - u_{\min})}{(\mu^*(x) - t_{\min})^r} \cdot (f(x) - t_{\min})^r + u_{\min} & \text{if } t \leq \mu^*(x), \\ -\frac{\frac{1}{2}(u_{\max} - u_{\min})}{(\mu^*(x) - t_{\max})^r} \cdot (f(x) - t_{\max})^r + u_{\max} & \text{if } t \geq \mu^*(x). \end{cases} \quad (5)$$

Comparing Fig. 3b with c, we see that our shade correction method has improved significantly. Previous methods of shade correction (Spencer et al., 1996; Frame et al., 1998; and Mendonça et al., 1999) are likely to produce false positives due to the darkening of regions close to bright patterns.

The presented method relies on the idea that bright, contrasted features are not part of the background. A more general approach for retinal image normalization based

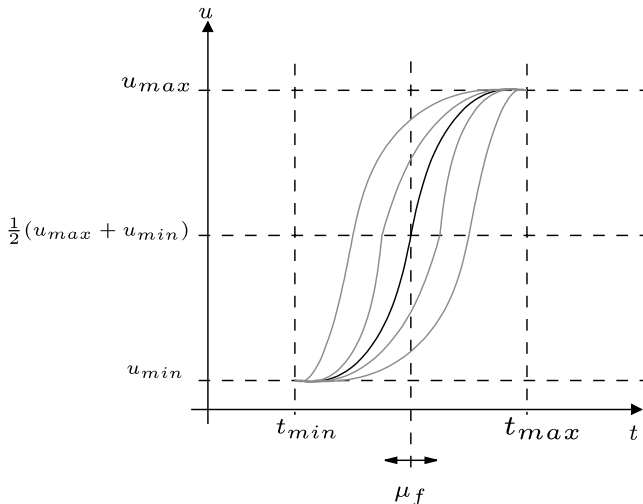


Fig. 2. The graph of the gray level transformation for different μ_f .

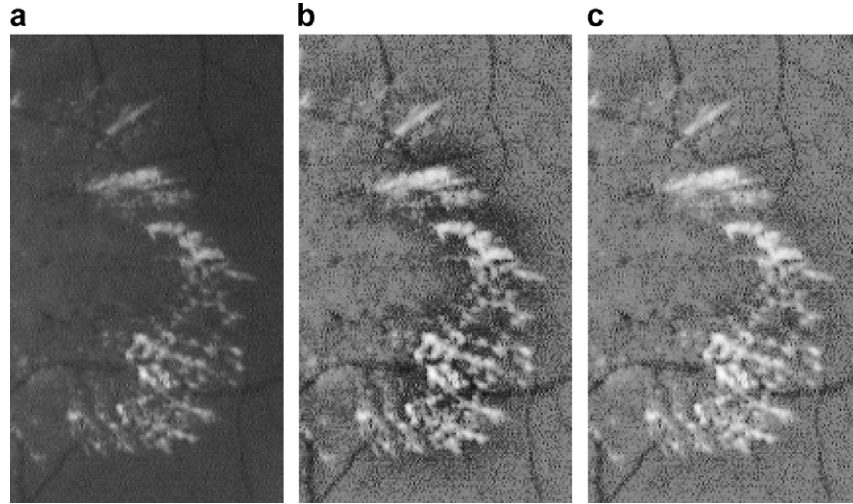


Fig. 3. The effect of filtering the background approximation: (a) original image, (b) shade correction and contrast enhancement using μ_t^w as background approximation and (c) shade correction and contrast enhancement using $\mu_{t_2}^w$ as background approximation.

on background detection has been proposed in Foracchia et al. (2005), it would be interesting to study the influence of these advanced image normalization techniques on the MA detection performance (see Fig. 4).

After having normalized the image, we apply a small Gaussian filter in order to attenuate the noise (width 5 pixels, $\sigma = 2$); it can be seen as a matched filter (Spencer et al., 1991). With G a Gaussian filter, we obtain the preprocessed image p by:

$$p = G * SC(f_g). \quad (6)$$

3.3. Detection of candidates by means of the diameter closing

The objective of this step is to find “candidates”, i.e. regions possibly corresponding to MA. According to its medical definition, a MA is a reddish, circular pattern with a diameter less than $125 \mu\text{m}$. As MA appear as dark patterns in the green channel (see Section 3.1), we aim at finding all dark patterns in the green channel with a diameter smaller than λ pixels (resolution dependent, here $\lambda = 9$ px); additional information is then used in the classification step. We think that this segmentation strategy is

the most appropriate one, as it is a direct translation of the medical definition of a MA.

The most straightforward method would be to adapt the method proposed in Lay (1983) to the green channel of color images, i.e. to calculate morphological closings ϕ^{L_i} with linear structuring elements L_i in different directions i (for definition of morphological operators, see (Soille, 1999; Serra, 1988)). The closing ϕ^{L_i} removes all dark features in an image which cannot contain the structuring element L_i of direction i . As for a properly chosen size of L_i , the MA cannot contain any of the structuring elements, independently of their direction, whereas the vessels can contain at least the structuring element in one direction, the operator $\phi^{\text{inf}} = \cap \phi^{L_i}$ removes only MA and not the vessels, supposed to be piecewise linear. However, in Spencer et al. (1996), the authors mention a limitation of this method: due to the limited number of considered directions, tortuous vessel like patterns may be treated like MA, as they cannot contain a structuring element either. The ideal operator would be $\phi^{\text{inf}} = \cap \phi^{B_i}$, with *all* structuring elements B_i having a diameter of λ pixels (or more). In this subsection, we propose an algorithm which overcomes this limitation. This method has first been published in Walter et al. (2001) and relies on the work of Vincent (1992) and Breen and Jones (1996).

First, we define the diameter α of a connected set X as its maximal extension:

$$\alpha(X) = \max_{x,y \in X} d(x,y) \quad (7)$$

with $d(x,y)$ the distance between two points $x,y \in X$. For simplicity, we use the block distance $d(x,y) = \max_{i=1 \dots n} |x_i - y_i|$ with $n = 2$ for 2D images.

With this definition of the diameter of a set, we can define a binary criteria opening (also called attribute based opening). A criterion κ assigns to each connected set A a

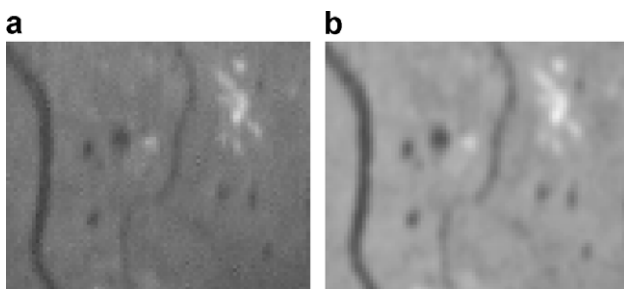
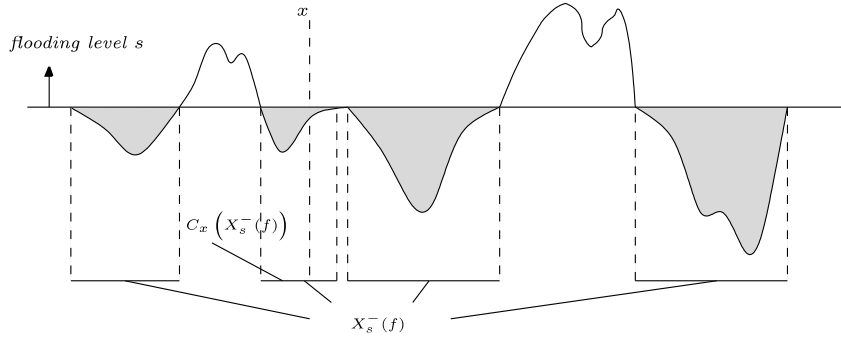


Fig. 4. Preprocessing step: (a) a detail of a fundus image containing MA and (b) detail of the preprocessed image.

Fig. 5. The flooding of an image f at level s .

binary value in accordance with a defined condition, i.e. $\kappa = 0$, if A does not meet the condition, and $\kappa = 1$ if it does. In this case, the criterion is $\kappa = 1$ if $\alpha(X_i) \geq \lambda$ and 0 if not.

Let X be an arbitrary binary image and X_i its connected components, i.e. $X = \cup X_i$ and $X_i \cap X_j = \emptyset$ for $i \neq j$. The diameter opening is the union of all connected components X_i with a diameter greater than or equal to λ :

$$\gamma_\lambda^\circ(X) = \bigcup_{\alpha(X_i) \geq \lambda} X_i. \quad (8)$$

As the applied criterion $\alpha(X_i) \geq \lambda$ is increasing¹ $\gamma_\lambda^\circ(X)$ is an opening; i.e. an idempotent ($\gamma_\lambda^\circ(X) = \gamma_\lambda^\circ[\gamma_\lambda^\circ(X)]$), increasing ($X \subseteq Y \rightarrow \gamma_\lambda^\circ(X) \subseteq \gamma_\lambda^\circ(Y)$) and anti-extensive ($\gamma_\lambda^\circ(X) \subseteq X$) operator.

It can be shown that for increasing binary criteria, the associated opening equals the supremum of openings with a family of structuring elements fulfilling the criteria (Serra, 1988). In particular, the diameter opening can be written as the supremum of all openings with structuring elements with a diameter greater than or equal to λ (Walter, 2003):

$$\gamma_\lambda^\circ(X) = \bigcup_{\alpha(B) \geq \lambda} \gamma^B(X). \quad (9)$$

The diameter closing acts in the same way on the inverted image X^c : it removes all holes $(X^c)_i$ (connected components of the background X^c) with a diameter smaller than λ . Furthermore, it can be written as the infimum of all morphological closings with structuring elements whose diameter is greater than or equal to λ :

$$[\phi_\lambda^\circ(X)](x) = X \cup \left(\bigcup_{\alpha((X^c)_i) < \lambda} (X^c)_i \right) = \bigcap_{\alpha(B) \geq \lambda} \phi^B. \quad (10)$$

We have now defined the diameter opening and closing for binary images. In order to pass from binary to gray level images, we can apply the binary operator to all level sets (the results of threshold operations for all gray levels t). Let $C_x(X)$ be the connected opening, i.e. the connected component of X containing x if $x \in X$ and the empty set if $x \notin X$. Furthermore, let $X_t^+(f)$ be the

section of f at level t , i.e. the set of all pixels for which $f(x) \geq t$ and $X_t^-(f)$ the section of the background (the “lakes”, see Fig. 5):

$$\begin{aligned} X_t^+(f) &= \{x | f(x) \geq t\}, \\ X_t^-(f) &= \{x | f(x) \leq t\}. \end{aligned} \quad (11)$$

Then, the gray scale diameter opening and closing can be defined respectively:

$$\begin{aligned} \gamma_\lambda^\circ(f) &= \sup\{s \leq f(x) | \alpha(C_x[X_s^+(f)]) \geq \lambda\}, \\ \phi_\lambda^\circ(f) &= \inf\{s \geq f(x) | \alpha(C_x[X_s^-(f)]) \geq \lambda\}. \end{aligned} \quad (12)$$

The diameter closing is therefore the ideal operator we have described above: it removes all dark patterns from a gray-scale image with a diameter smaller than λ , and can be seen as the infimum of all closings with structuring elements with diameter greater than or equal to λ . In this sense, the operator is optimal and a generalization of the approximative method proposed in Laÿ (1983) used by the majority of authors, where only linear structuring elements fulfilling the criterion are used.

Criteria based operators can be implemented efficiently by flooding simulation (Vincent, 1992; Breen and Jones, 1996). The principle is as follows: the flooding starts with the lowest local minima in the image (i.e. with the global minima). Let s be the actual flooding level (in the beginning this is the value of the global minima). First, we determine the diameter of all the lakes with gray level s . If the diameter of a lake exceeds λ , the output image takes the value s for all the points belonging to this lake (“the flooding stops for this lake”). Then s is incremented, the new local minima at this level are identified, all lakes with gray levels smaller than or equal to s are extended until there is no more pixel x in the image with $f(x) \leq s$ not having been processed (i.e. not belonging to a lake). If two lakes meet, they fuse and the resulting lake is considered as one lake from now on. Then, when the flooding has been finished for this level, the diameter of all lakes are calculated. If the diameter of a lake exceeds or equals λ for the first time (i.e. in previous tests, $\alpha(X_i) < \lambda$) the output image is set to s for all the pixels of this lake. In this way, the whole image is flooded until there is no more lake with a diameter small-

¹ Let A, B be two connected sets. If $A \subseteq B$ implies that if A fulfills κ , B also fulfills κ , then κ is called an increasing criterion.

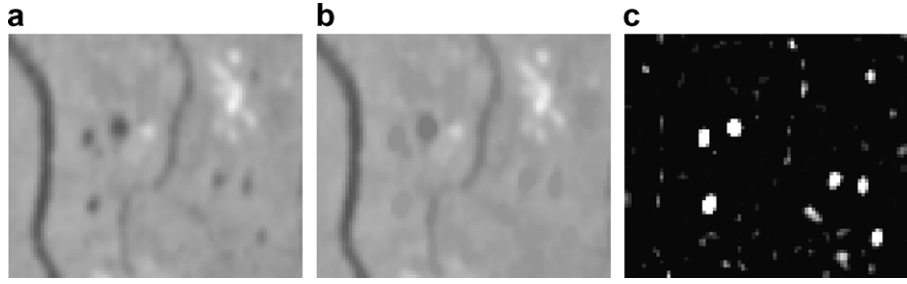


Fig. 6. Detection of dark details by means of the diameter closing: (a) the preprocessed image, (b) the diameter closing and (c) the associated top-hat transformation.

ler than λ . This algorithm can be implemented very efficiently with hierarchical queues.

In Fig. 6, we show the application of the diameter closing to the detection of MA. The preprocessed image is shown in Fig. 6a; its closing by diameter in Fig. 6b. We note that MA are mostly removed from the image, whereas vessel like patterns of the same width remain nearly unchanged. The associated top-hat $\phi_\lambda^\circ f - f$ is shown in Fig. 6c. We see that MA are the patterns with highest contrast, but there exist also other patterns fulfilling the size criteria. From this image, candidates can be extracted by a global threshold.

However, the choice of a global threshold is not an easy task. Different methods have been proposed: fix threshold (Autio et al., 2005), histogram based thresholds (Spencer et al., 1996; Zana, 1999); in Walter and Klein (2002), the authors propose a mixture of both. We have experienced that a threshold which does not take into consideration image properties does not yield satisfying results, because depending on the image quality, too many candidates may be segmented, resulting in very asymmetric class distributions or too many real MA are missed. The underlying idea of a histogram based threshold is that only a certain number of candidates is reasonable, i.e. we do not expect the number of MA to be several hundreds, for instance. This means that an image dependent threshold aims at controlling somehow the number of candidates. If there is a high amount of noise, the threshold should be higher in order not to segment too many false positives; if the image suffers from low contrast (and so do the MA), the threshold should be lower in order to still achieve acceptable sensitivity. We have found that these considerations are closely related to the number of candidates we expect. We therefore propose a threshold which gives as a result at least K candidates. If there is no threshold resulting in at least K candidates, we choose the threshold giving the maximum number of candidates.

However, a threshold based entirely on the histogram does always segment candidates, whereas there may not be any in the image. We therefore adapt a hybrid threshold scheme: we bound the threshold range to $T_l \leq T \leq T_u$. The values T_l and T_u have been found experimentally: $T_l = 15$ and $T_u = 20$. These settings depend much on the chosen preprocessing method and its parameters.

$$T'_K = \begin{cases} \min t & \text{with } CC(X_t^+) \geq K, \\ \min t & \text{with } \forall \tau \neq t, K > CC(X_t^+) \geq CC(X_\tau^+), \end{cases}$$

$$T_K = \begin{cases} T_l & \text{if } T'_K < T_l, \\ T'_K & \text{if } T_l \leq T'_K \leq T_u, \\ T_u & \text{if } T'_K > T_u \end{cases} \quad (13)$$

with $CC(A)$ the number of connected components of set A .

In order to obtain a more representative region area, we apply a double threshold. Let T_K be the threshold segmenting at least K connected components (13), and $X_{T_K}^+$ the resulting binary image. Furthermore, let $R_X(Y)$ be the morphological reconstruction by dilation (Soille, 1999) of marker Y under image X . Then, we obtain the candidate image by:

$$C = R_{X_{T_K}^+}^+(X_{T_K}^+). \quad (14)$$

3.4. Feature extraction

We have used 15 features in order to distinguish real MA from false positives (FP). We distinguish three types of features:

- Binary features like size and shape of the candidate regions.
- Gray-level features based on the gray level distribution of a gray-scale image within the candidate region.
- Color features based on the color within the candidate region.

In previous versions of this algorithm, we have used less features: 5 in Walter and Klein (2002), 9 in Walter (2003). In the following, C_i denotes the candidate region (a set of points) with index i , f the green channel, p the preprocessed image, ϑ the top-hat transform associated to the diameter closing of the preprocessed image $\vartheta = \phi_\lambda^\circ(p) - p$.

Furthermore, we calculate a morphological top-hat image $\phi^{sB}p - p$. This image contains all dark patterns which are too small to contain the structuring element sB , i.e. the vascular patterns as well as hemorrhages, MA, and other objects. From this image, we remove all patterns with maximal extension λ and we obtain $v = \gamma_\lambda^\circ(\phi^{sB}p - p)$.

Using these images (f , p , ϑ and v), we can define the following features:

- (1) The surface (number of pixels of the candidate region).
- (2) *The circularity* helps distinguishing between circular and elongated objects: $\frac{4 \cdot \text{Surf}(C_i)}{\pi \cdot (\alpha(C_i))^2}$.
- (3) *The maximal value of the top-hat by diameter ϑ* is a contrast measure (the depth of the flooded lake).
- (4) *The mean value of the top-hat ϑ* corresponds to the average contrast on the candidate region (mean depth of the lake).
- (5) *The dynamic* is a classical morphological contrast measure (Soille, 1999) (in the flooding procedure, the dynamic corresponds to the minimal grey level for which the minimum disappears).
- (6) *The outer mean value of p* adds information about the surroundings of the candidate. We define the surroundings of a candidate C_i as $Ex(C_i) = \delta^{3B} C_i \setminus \delta^B C_i$, with $\delta^B A$ the morphological dilation of set A with the structuring element B . On this region, we calculate the mean value of the preprocessed, normalized image $p(x)$ (in contrary to contrast measures, this feature only makes sense if calculated on the normalized image).
- (7) *The outer standard deviation of p* gives information about the grey level variation within the surroundings of the candidate.
- (8) *The inner standard deviation of p* .
- (9) *The inner mean value of v* helps identifying candidates situated on vessels. This value is supposed to be relatively low for isolated patterns.
- (10) *The inner mean value of v* also helps identifying candidates situated on vessels.
- (11) *The inner range* is simply the dynamic range of the preprocessed image p in the candidate region ($\max_{C_i} p - \min_{C_i} p$) and exploits the information about smoothness of the transition between the candidate and the environment.
- (12) *The outer range* is the dynamical range of the preprocessed image p on the surroundings of the candidates ($\max_{Ex(C_i)} p - \min_{Ex(C_i)} p$).
- (13) *The gray level contrast between inner and outer region* are the most discriminative features. They are calculated as the difference between the mean on the candidate C_i and on its surroundings $Ex(C_i)$.
- (14) *The color contrast* is the only feature which is not exclusively based on the green channel. We have tested several color features, but the only one which has been found useful, was the contrast in the *Lab* space, defined as the sum of the squared differences between candidate region and surroundings: $(\mu_{\text{ext}}(L) - \mu_{\text{int}}(L))^2 + (\mu_{\text{ext}}(a) - \mu_{\text{int}}(a))^2 + (\mu_{\text{ext}}(b) - \mu_{\text{int}}(b))^2$, with μ_{int} the mean value on the candidate regions and μ_{ext} the mean value on the surroundings.
- (15) *Half-range area* is the number of pixels inside the candidate region with a grey level greater than the

arithmetical mean of minimum and maximum in the candidate region. It gives additional information about the grey level distribution of the micro-aneurysm.

Besides these features, we have tested many other features, but the tests showed that they did not significantly enhance performance. For instance, the contrast measure 13 could be calculated in different images, like different color channels, the original image, the preprocessed image, etc., but we did not find them improving the discriminative power of our feature set. The same holds for the mean value of non-normalized images.

The extracted features have very different ranges and values; it is therefore necessary to normalize them in such a way that their mean value is 0 and their variance is 1.

Now each candidate is characterized by a vector z in a 15-dimensional feature space; the final step is now to decide whether a candidate is a real MA or a false positive knowing its representation z . This step is presented in the next section.

3.5. Classification

The problem is to assign to each candidate, represented by the P -dimensional vector z (here $P = 15$), one of the two classes ω_1 (MA) or ω_2 (not MA).

In order to achieve this, we first establish a training set, i.e. a set of candidates for which the feature vector and the classification result are known:

$$TRAIN = \{(z_i, \omega_k^{(i)}) | i = 1, \dots, N, k = 1, 2\}$$

The classification task consists in deriving a general classification rule for unknown candidates from this training set. There exist many methods to solve this kind of problems; to the detection of MA, the k -nearest-neighbor (KNN) method (Walter et al., 2001; Niemeijer et al., 2005), support vector machines (Autio et al., 2005), linear discriminant analysis (Grisan and Ruggeri, 2005), rule based analysis and neural networks (Frame et al., 1998) have been applied.

The choice of an appropriate method has two important aspects: first, the method should be robust against outliers in the training set, because it is very difficult to obtain an absolutely reliable ground truth. Second, the distribution of the features is unknown.

These considerations have lead several authors to the use of KNN classifiers (Walter et al., 2001; Niemeijer et al., 2005), which consist in assigning to a new candidate z the class to which the majority among the K nearest neighbors of z belongs. The advantages of this method are that for K reasonably large, the method becomes robust against outliers and that it is non-parametric (i.e. no assumption about the feature distribution must be made). One drawback of the method is that all neighbors have the same weight for the decision, independently of their distance from the candidate to classify. Moreover, the method might not work properly if the training set is very asym-

metric for the two classes (i.e. if the sample number of one class is much larger than the sample number from the other class), particularly for large K . In order to overcome these problems and to meet the requirements discussed above, we have chosen the kernel method for density estimation, combined with Bayesian risk minimization (Webb, 2002; Comaniciu et al., 2001; Fricout and Jeulin, 2004; Hastie et al., 2000).

The Bayesian risk minimization rule for a two-class problem assigns a candidate z to class ω_1 if:

$$\frac{p(z|\omega_1)}{p(z|\omega_2)} > \frac{\lambda_{21}p(\omega_2)}{\lambda_{12}p(\omega_1)} = \mu, \quad (15)$$

where $p(\omega_k)$ is the a priori probability of class ω_k , $p(z|\omega_k)$ the class-conditional probability density function and λ_{ij} the cost of assigning a pattern to class ω_i under the condition that it belongs to class ω_j . The teaching (determining the classifier parameters) consists in finding a reasonable value for μ and in estimating the class conditional probability densities $p(z|\omega_k)$ from the training set. In order to find optimal parameters for the classifier, only the training set is to be used.

The kernel density estimation makes very few assumptions about the real underlying distribution and is therefore suitable for this task. The multivariate fixed bandwidth kernel density estimate \hat{p} of a distribution p is given by Comaniciu et al. (2001):

$$\hat{p}(z) = \frac{1}{Nh^p} \sum_{i=1}^N K\left(\frac{z - z_i}{h}\right) \quad (16)$$

with K the *kernel function*, which integrates to 1, and h a parameter, which is called the *bandwidth* of the kernel. Different kernels can be used, the Gaussian kernel seems a reasonable choice:

$$K(z) = \frac{1}{\sigma\sqrt{2\pi}} \exp\left(-\frac{1}{2}\left(\frac{|z|}{\sigma}\right)^2\right). \quad (17)$$

A rather difficult problem is the choice of h , which can be understood as a smoothing parameter controlling the trade-off between variance and bias of the estimation.

For low bandwidths h (narrow kernels), we obtain high variance and low bias, for large bandwidths h (broad kernels), we obtain low variance at the cost of important smoothing (high bias) (Comaniciu et al., 2001). Moreover, the feature density is not uniform, and an ideal h for one part of the feature space may not be ideal for another part. One possibility to overcome this problem is to choose the bandwidth depending on z (balloon estimators) or depending on z_i (point estimators); the latter ones have been shown to be more efficient (Comaniciu et al., 2001). The idea is to use large bandwidths in regions with low sample density in order to obtain a smooth estimation, and to use low bandwidths in high density regions. We have tried several automatic bandwidth selection methods; we obtained satisfactory results with a bandwidth determined by

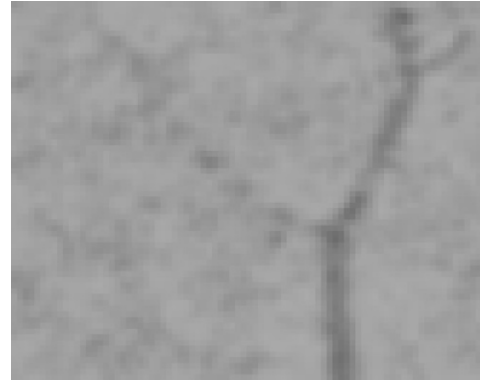


Fig. 7. Small vessels can appear as a succession of small isolated patterns, which could be detected as false positives.

$$h(z_i) = \frac{1}{1 + n_{z_i}(d)}, \quad (18)$$

where $n_{z_i}(d)$ is the number of neighbors of z_i within a radius of $d = 0.5$ (the features have been normalized to have a mean of 0 and a variance of 1). With this bandwidth $h(z_i)$ for every point of the training set, we can estimate the class conditional density $p(z|\omega_k)$ for ω_1 and ω_2 , respectively (Eq. (16)).

The compromise between sensitivity and specificity can be adjusted by varying parameter μ ; we have chosen $\mu = 1.5$.

Postprocessing: Our segmentation method has been designed in order to extract only small patterns, i.e. patterns whose maximal extension does not exceed a certain value. In particular, the method makes the distinction between vessel-like patterns and small dark patterns, possibly corresponding to MA. However, small vessels appear sometimes as a succession of small circular patterns. In this case, they are segmented and sometimes classified as MA, as they are visually very similar to MA. As a matter of fact, they cannot be removed by the use of their local properties: it is only by the way they are arranged in the image, that they can be identified (see an example in Fig. 7). We therefore propose a postprocessing step, in order to remove all candidates situated on vessels (for vessel detection, see Zana and Klein, 2001; Staal et al., 2004; Walter and Klein, 2005).

The results of this algorithm (with or without the postprocessing step) are shown in the next section.

4. Results

4.1. Training set and test set

One of the major problems in the detection of MA is to establish a “gold standard”, i.e. a set of annotated images for learning (training set), and another for testing purposes (test set). MA can easily be confounded with other patterns; the manual results are therefore rather subjective. In this study, we have used a training set of 21 images. In all images of the training set, there was at least 1 MA.

Table 1
Comparison between the human graders and the ground truth

	Reader A	Reader B	Reader C
Sensitivity in %	75.8	82.8	87.8
FP per image	0.59	2.97	0.80

Moreover, 11 images showed exudates, 12 hemorrhages. The test set consisted of 94 images out of which 68 contained at least 1 MA. In 29 images, exudates were present, in 27 there were hemorrhages. 26 images did not show any form of DR.

In order to obtain a “gold standard”, i.e. a reference which can be seen as ground truth, we have asked three different ophthalmologists to grade the images independently. In order to guarantee the same grading conditions, we fixed a protocol allowing neither zoom nor image manipulation (like contrast enhancement or brightness control). Furthermore, we made sure that neither the training nor the test set contained images with more than 20 MA, because we have observed that the sensitivity decreased for all graders when there were many MA. For such images, it is hard to establish a ground truth.

Taking the mean of the three grading results does not necessarily give something closer to the truth than the result obtained by any of the graders. Therefore, we asked the three experts to discuss their results and to find a consensus for every candidate on which they had disagreed in the first reading. Candidates for which they could not find a consensus were marked as doubtful cases; these candidates do not appear in the final statistics. The result of this discussion was considered as sufficiently confident to establish a “gold standard” to which the automatic method could be compared.

In order to estimate the performance of a human reader (and thus the difficulty of the problem), we compared the

three independent readings to the ground truth. The results are shown in Table 1.

4.2. Comparison of the automatic result with the gold standard

There are two different levels of evaluation: the lesion level and the image level. In this paper, we discuss both evaluation levels, but we focused on the lesion level, because we do not present a whole system of automatic diagnosis, but only a part of it; it is therefore most informative to see how good the detection of these lesions really is.

For the 94 images of the test set, we have compared our algorithm to the gold standard. The segmentation algorithm gave 8837 candidates, containing 373 MA, 92 doubtful objects (which were discarded) and 8372 false positives. After classification, 332 out of 373 MA were correctly identified, yielding a sensitivity of 89.0%, the average number of false positives being 2.92 FP per image. From the 41 missed MA, 4 were already missed by the segmentation step. The algorithm with postprocessing (i.e. with removal of the vessels) gave a sensitivity of 88.47% with an average number of 2.13 FP per image. The performance of the two methods (with and without removal of vessels) is illustrated in Fig. 8 for different values of the average number of FP per image.

We compared these results to the performance of a *KNN* classifier and a Gaussian classifier, i.e. Bayesian risk-minimizing classifier with normal density estimation using diagonal class-dependent covariance matrices, which we found to perform better than the normal-based linear classifier (pooled covariance-matrix for all classes). The FROC of the Gaussian classifier and of the *KNN* classifier are shown in Fig. 8. The three classification methods (kernel method, gaussian classifier and *KNN*) give rather similar results for a working point around a sensitivity of 65% with 1.4 FP per image, but this situation changes when a sensitivity of

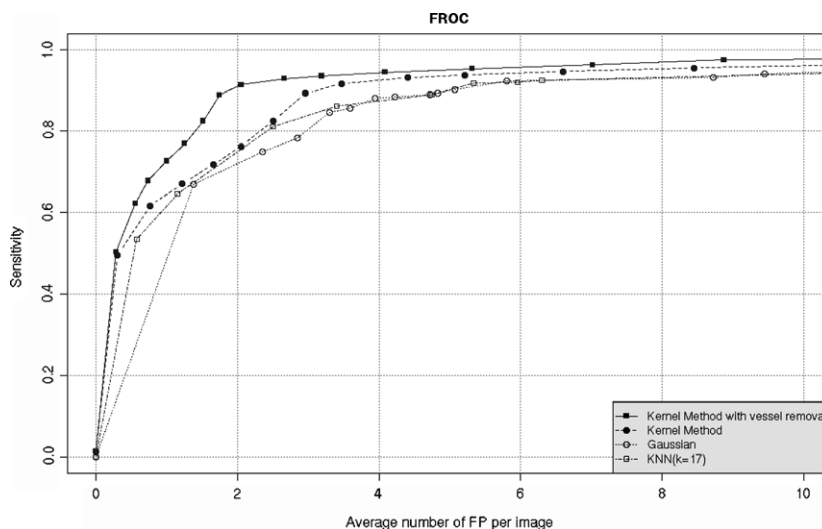


Fig. 8. Free receiver operating curve (FROC) for our algorithm with or without vessel removal. These curves are compared to the FROC of a Gaussian classifier (quadratic, with linear covariance matrix).

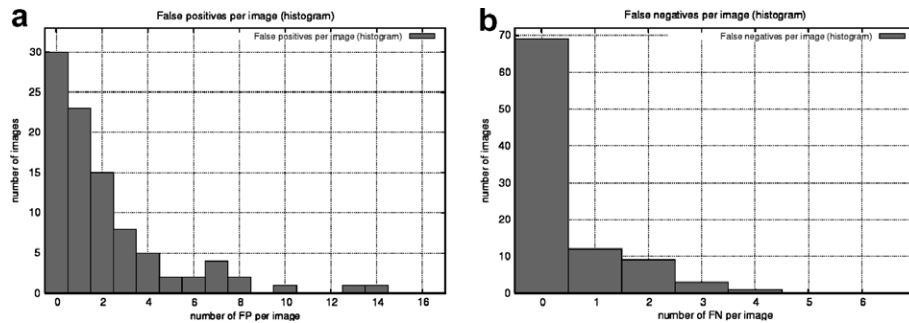


Fig. 9. Error distribution: number of images vs. number of FP (a) and FN (b).

around 90% is required. In this case, the Bayesian classifier based on kernel density estimation outperforms the *KNN* and the Gaussian classifier for our test set.

Studying the per image error distributions for false positives and false negatives, we can interpret these results in more detail. In Fig. 9a, we show the number of images (*y*-axis), for which we obtained 0, 1, 2, ..., FP. We see that in 30 images, there are no FP, in 53 images less than 2. We also see that more than 25% of all false positives are concentrated in 5 images. The reason is that these images were noisy. We note that it can never be excluded that some image shows an abnormally high number of false positives; the most important aspect however is that for the large majority of images, we obtain no or only few false positives.

For the FN-distribution, the plot in Fig. 9b shows that in 69 of 94 images, we do not miss any MA and that in all images but three, we do not miss more than 2 MA.

In 68 out of 94 images, there is at least one MA present. For 66 of these images, the automatic algorithm detects at least one MA (sensitivity of 97.0%); the two images which can be considered as FN show both a very mild form of DR with exactly one MA, which has not been detected by the automatic algorithm. Among the 26 images without MA, the automatic algorithm classifies 18 correctly; in 3 images, the automatic algorithm detects 1 FP, in 4 images 2 FP and in one image 10 FP.

5. Conclusion

In this paper, we have presented a method of automatic detection of MA, based on diameter closing and kernel density estimation for automatic classification. We have tested this algorithm on a set of 94 images and we have obtained a sensitivity of 88.47% with 2.13 FP per image.

Although further evaluation of this algorithm on larger populations is still required, these results are satisfying. Any serious form of DR is unlikely to be missed and this should make ophthalmologists confident in using this automatic method; the moderate number of FP should not increase too much the burden of image grading.

In order to come to a clinical application, the proposed method will be combined with an algorithm for the detection of hemorrhages and an algorithm for the detection of exudates.

References

- Autio, I., Borrás, J.C., Immonen, I., Jalli, P., Ukkonen, E., 2005. A voting margin approach for the detection of retinal microaneurysms. In: *Proceedings: Visualization, Imaging and Image Processing*, Spain, September.
- Breen, E.J., Jones, R., 1996. Attribute openings, thinnings and granulometries. *Computer Vision and Image Understanding* 64 (3), 377–389.
- Comaniciu, D., Ramesh, V., Meer, P., 2001. The variable bandwidth mean shift and data-driven scale selection. In: *8th International Conference on Computer Vision*, vol. I, Vancouver, Canada, July, pp. 438–445.
- Delori, F.C., Pflibsen, K.P., 1989. Spectral reflectance of the ocular fundus. *Applied Optics* 28, 1061–1071.
- Duda, R.O., Hart, P.E., 1973. *Pattern Recognition and Scene Analysis*. Wiley-Interscience.
- Grisan, E., Ruggeri, A., 2005. A hierarchical Bayesian classification for non-vascular lesions detection in fundus images. In: *EMBECC'05, 3rd European Medical and Biological Engineering Conference*, Prague, November, pp. 20–25.
- Frame, A.J., Undill, P.E., Cree, M.J., Olson, J.A., McHardy, K.C., Sharp, P.F., Forrester, J.F., 1998. A comparison of computer based classification methods applied to the detection of microaneurysms in ophthalmic fluorescein angiograms. *Computers in Biomedical Research* 28, 225–238.
- Fricout, G., Jeulin, D., 2004. Texture classification from their morphological properties. In: *Proceedings of the 9th International Conference on Metrology and Properties of Engineering Surfaces*, April.
- Foracchia, M., Grisan, E., Ruggeri, A., 2005. Luminosity and contrast normalization in retinal images. *Medical Image Analysis* 9 (3), 179–190.
- Hastie, T., Tibshirani, R., Friedman, J., 2000. *The Elements of Statistical Learning*. Springer, ISBN 0-387-95284-5.
- Hellstedt, T., Immonen, I., 1996. Disappearance and formation rates of microaneurysms in early diabetic retinopathy. *British Journal of Ophthalmology* 80 (2), 135–139.
- Klein, R., Klein, B.E., Moss, S.E., 1992. The epidemiology of ocular problems in diabetes mellitus. *S.S.Feman: Ocular Problems in Diabetes Mellitus* 1, 1–51.
- Klein, R., Meuer, S.M., Moss, S.E., Klein, B.E., 1995. Retinal microaneurysm counts and 10-year progression of diabetic retinopathy. *Archives of Ophthalmology* 113 (11), 1386–1391.
- Lay, B., 1983. *Analyse automatique des images angiofluorographiques au cours de la rétinopathie diabétique*. Ph.D. Thesis, Centre de Mathématique Morphologie, Paris School of Mines, June.
- Lee, S.C., Lee, E.T., Kingsley, R.M., Wang, Y., Russell, D., Klein, R., Warn, A., 2001. Comparison of diagnosis of early retinal lesions of diabetic retinopathy between a computer system and human experts. *Archives of Ophthalmology* 119, 509–515.
- Massin, P., Erginay, A., Gaudric, A., 2000. *Rétinopathie Diabétique*. Elsevier, ISBN 2-84299-194-X.
- Massin, P., 2002. *Dépistage de la Rétinopathie Diabétique – Aspects techniques et organisationnels*. Ph.D Thesis, Paris VII.

- Mendonça, A.M., Campilho, A.J., Nunes, J.M., 1999. Automatic segmentation of microaneurysms in retinal angiograms of diabetic patients. In: Proc. IEEE International Conference of Image Analysis Applications (ICIAP 99), pp. 728–733.
- Moreno Barriuso, E., 2000. Laser ray tracing in the human eye: measurement and correction of the aberrations by means of phase plates. Ph.D. Thesis, Institute Of Optics, CSIC, Spain, June.
- Niemeijer, M., van Ginneken, B., Staal, J., Suttorp-Schulten, M.S.A., Abramoff, M.D., 2005. Automatic detection of red lesions in digital color fundus photographs. *IEEE Transactions on Medical Imaging* 24 (5), 584–592.
- Øien, G.E., Osnes, P., 1995. Diabetic retinopathy: automatic detection of early symptoms from retinal images. In: Proc. Norwegian Signal Processing Symposium, September, pp. 135–140.
- Papageorgiou, C.P., Oren, M., Poggio, T., 1998. A general framework for object detection. In: ICCV'98: Proceedings of the Sixth International Conference on Computer Vision, pp. 555–562.
- Preece, S.J., Claridge, E., 2001. Monte Carlo modelling of the spectral reflectance of the human eye. *Physics in Medicine and Biology* 47, 2863–2877.
- Serra, J., 1988. *Image Analysis and Mathematical Morphology*. Academic Press.
- Soille, P., 1999. *Morphological Image Analysis: Principles and Applications*. Springer, Berlin, Heidelberg, New York.
- Spencer, T., Phillips, R.P., Sharp, P.F., Forrester, J.V., 1991. Automated detection and quantification of microaneurysms in fluorescein angiograms. *Graefe's Archive for Clinical and Experimental Ophthalmology* 230, 36–41.
- Spencer, T., Olson, J.A., McHardy, K.C., Sharp, P.F., Forrester, J.V., 1996. An image processing strategy for the segmentation and quantification of microaneurysms in fluorescein angiograms of the ocular fundus. *Computers in Biomedical Research* 29, 284–302.
- Staal, J.J., Abrámoff, M.D., Niemeijer, M., Viergever, M.A., van Ginneken, B., 2004. Ridge based vessel segmentation in color images of the retina. *IEEE Transactions on Medical Imaging* 23 (4), 501–509.
- Vincent, L., 1992. Morphological area openings and closings for grayscale images. *NATO Shape in Picture Workshop*, Driebergen, pp. 197–208.
- Viola, P., Jones, M., 2004. Robust real-time face detection. *International Journal of Computer Vision* 57, 137–154.
- Walter, T., Klein, J.-C., 2001. Segmentation of color fundus images of the human retina: detection of the optic disc and the vascular tree using morphological techniques. In: Crespo, J., Maojo, V., Martin, F. (Eds.), *Lecture Notes in Computer Science (LNCS)*, vol. 2199, pp. 282–287.
- Walter, T., Klein, J.-C., 2002. Automatic detection of microaneurysms in color fundus images of the human retina by means of the bounding box closing. In: Colosimo, A., Giuliani, A., Sirabella, P. (Eds.), *Lecture Notes in Computer Science (LNCS)*, vol. 2526, pp. 210–220.
- Walter, T., 2003. Application de la Morphologie Mathématique au diagnostic de la Rétinopathie Diabétique à partir d'images couleur. Ph.D. Thesis, Centre of Mathematical Morphology, Paris School of Mines, September.
- Walter, T., Klein, J.-C., 2005. Automatic analysis of color fundus photographs and its application to the diagnosis of diabetic retinopathy. In: Suri, J., Wilson, D., Laxminarayan, S. (Eds.), *Handbook of Biomedical Image Analysis: Segmentation Models*, vol. 2. Kluwer Academic/Plenum Publishers, pp. 315–368 (Part B, Chapter 7).
- Webb, A., 2002. *Statistical Pattern Recognition*. Wiley, ISBN 0-470-84514-7.
- Zana, F., 1999. Une approche morphologique pour les détections et Bayésienne pour le recalage d'images multimodales: application aux images rétinienne. Ph.D. Thesis, Centre of Mathematical Morphology, Paris School of Mines, May.
- Zana, F., Klein, J.-C., 2001. Segmentation of vessel-like patterns using mathematical morphology and curvature evaluation. *IEEE Transaction on Image Processing* 10 (7), 1010–1019.

Further reading

- Sinthanayothin, C., Boyce, J.F., Cook, H.L., Williamson, T.H., 1999. Automated localisation of the optic disc, fovea and retinal blood vessels from digital colour fundus images. *British Journal of Ophthalmology* 83 (8), 231–238.